Measured Emittance Dependence on the Injection Method in Laser Plasma Accelerators

S. K. Barber,[1,*] J. van Tilborg,[1] C. B. Schroeder,[1] R. Lehe,[1] H.-E. Tsai,[1] K. K. Swanson,[1,2] S. Steinke,[1] K. Nakamura,[1] C. G. R. Geddes,[1] C. Benedetti,[1] E. Esarey,[1] and W. P. Leemans[1,2]

[1]*Lawrence Berkeley National Laboratory, University of California, Berkeley, California 94720, USA*

[2]*Department of Physics, University of California, Berkeley, California 94720, USA*

(Received 16 March 2017; published 5 September 2017)

Single-shot, charge-dependent emittance measurements of electron beams generated by a laser plasma accelerator (LPA) reveal that shock-induced density down-ramp injection produces beams with normalized emittances a factor of 2 smaller than beams produced via ionization injection. Such a comparison is made possible by the tunable LPA setup, which allows electron beams with nearly identical central energy and peak spectral charge density to be produced using the two distinct injection mechanisms. Parametric measurements of this type are essential for the development of LPA-based applications which ultimately require high charge density and low emittance.

DOI: 10.1103/PhysRevLett.119.104801

Owing to their ability to accelerate electron beams to GeV-class energies over centimeter-scale distances with femtosecond-scale bunch durations and ultralow emittances [1], laser plasma accelerators (LPAs) are poised to usher in a new era of compact accelerator driven applications. Compact LPA-based x-ray free-electron lasers [2–5], compact monoenergetic MeV-class Thomson-scattered photons [6,7], and progress towards an LPA-based electron-positron collider [8] are being actively pursued. Most LPA-based applications require excellent 6D electron beam brightness, defined as $B_{6D} = I_b/(\sigma_E \epsilon_x \epsilon_y)$, where I_b is the peak beam current, σ_E is the energy spread, and $\epsilon_{x,y}$ are the normalized transverse emittances (herein referred to simply as emittance). Although a key critical parameter, to date very few direct emittance measurements have been carried out, perhaps owing to the typical percent-level energy spreads and challenges of LPA stability and tunability. Besides indirect techniques based on spectral analysis of x-ray betatron or Compton radiation [9–11] (which rely on various assumptions, simulations, and complex analysis to unravel the e-beam source properties), traditional knife scans and pepperpot measurements are limited in their utility [12]. Only Weingartner *et al.* [13] performed direct post-LPA emittance characterization by combining conventional quadrupole focusing techniques and the energy-dispersed plane of a magnetic spectrometer (a technique also recently applied in electron-beam-driven plasma wakefield acceleration experiments [14]). While impressively demonstrating $\epsilon \simeq 0.21$ mm mrad, little was done to explore parametric dependences of the emittance.

In this Letter we combine a stable and tunable LPA, followed by a quadrupole triplet and an energy-dispersed magnetic spectrometer, all in a resolution-optimized geometry to perform parametric studies on the LPA emittance. We present a direct comparison of emittance measurements of electron beams generated by two different injection mechanisms: ionization injection [15–19] and shock-induced density down-ramp injection [20–25]. Both schemes have attracted recognition as a path towards localized and controllable injection, and direct energy-dispersed emittance measurements have so far not been measured. In the former case, a high intensity laser $a > 2$ ionizes and drives a wake in a high-Z-doped gas, with a the normalized laser strength [1]. The inner-shell electrons that eventually get trapped are only ionized near the peak of the laser at time t_i and will experience a transverse ponderomotive kick that will contribute to increased emittance. In addition, in the polarization plane, a residual transverse momentum $p_\perp/m_e c \approx a(t_i)$ will contribute as well. In the density down-ramp injection scheme, a wake driven in a preformed plasma crosses a transition from high to low density plasma. At this crossing, a decrease in the local phase velocity of the wake relaxes the threshold for trapping electrons. Density down-ramp injection in the nonlinear bubble regime is considerably complex due in large part to the plasma density spike at the point of injection near the back of the bubble. From simulations it is clear, however, that in contrast to ionization injection, the trapped electrons originate from a much more selective area in the background electron's phase space (and thus obtain a lower emittance).

The two configurations of the LPA were tuned and optimized to deliver beams with the same central energy and peak spectral charge density (charge/MeV), thus enabling evaluation of one injection method versus the other. The down-ramp method yielded $\epsilon = 1$ mm mrad at application-relevant charge densities up to 2 pC/MeV, and doubled for the ionization-injected beam. In both schemes a clear relation between charge density and emittance was recorded. These results mark a major step forward in characterizing and comparing LPA sources produced by different injection mechanisms. The LPA community's variety in injection mechanisms, plasma targets, and laser parameters offers the opportunity for further source optimization to enable exciting applications.

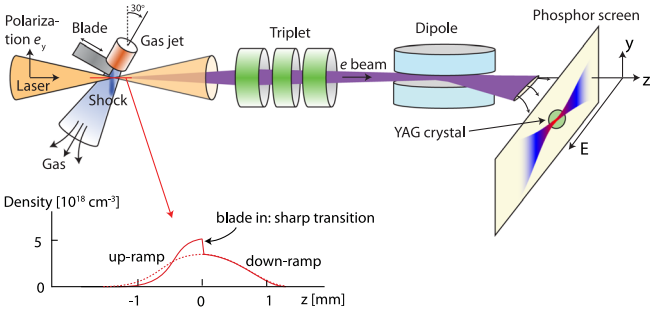

FIG. 1. Schematic representation of the LPA setup consisting of a supersonic gas jet and adjustable blade used for density profile tuning in the down-ramp configuration. Electrons generated by the focused laser pulse are captured and focused by a PMQ triplet onto the spectrometer screen. which is equipped with a large energy bandwidth, phosphor-screen-based diagnostic used for initial electron beam characterization, and a high-resolution, narrow bandwidth YAG crystal-based diagnostic used for emittance measurements.

The experiment, shown schematically in Fig. 1, was carried out at the BELLA Center using the TREX Ti:sapphire laser which delivered 1.8 J pulses of 45 fs FWHM duration that were focused by a 2.0 m focal length off-axis parabola to spot sizes of $w_0 = 22$ μm. The target used for both injection schemes was a supersonic gas jet with 840 μm diameter [25–27]. In the case of ionization injection, a mixture of 99% helium and 1% nitrogen was used, and for the down-ramp configuration pure hydrogen was used. In order to produce the density down-ramp, a thin blade impinged the gas flow, generating a shock that induced a density transition from 5.0×10^{18} to 2.5×10^{18} electrons/cm^3 over a length of $\sim$100 μm. The adjustability of the blade position allowed precise tunability of the central energy of the electron beams by adjusting the effective accelerator length. For ionization injection, without the blade, the accelerator length, and thus central energy, was tuned by introducing a small transverse offset between the laser and gas jet center. Using these methods, the two LPA configurations were optimized to deliver stable electron beams with a central energy of 57 MeV and rms energy spreads of 4 and 12 MeV for down-ramp and ionization, respectively. Shot-to-shot rms variation of the central energy was 2 and 7 MeV, respectively. Because the down-ramp configuration by default produced beams with significantly higher spectral charge density at 57 MeV, it was necessary to slightly reduce the laser intensity by enlongating the pulse by increasing the grating separation in the compressor, which reduced the charge density without significant change in the energy distribution.

The electron beam transport line used for the emittance measurements consisted of a permanent magnet quadrupole (PMQ) triplet and a magnetic spectrometer dipole. The distance from the LPA source to the first PMQ magnet in the triplet was 17 cm. Details of the triplet used in this experiment are well described in Table I of Ref. [28]. Note that we used this triplet in the reverse configuration such that the LPA beam sees Q3 first (resulting in a sign flip of the field gradients). From the exit of the triplet, the beam drifted 1.73 m before entering the spectrometer dipole. At 57 MeV, the bend angle was 0.43 rad with a 88 cm bend radius. Finally, after the dipole, the beam drifted a final 22 cm before hitting a charge calibrated, 300 μm thick scintillating Ce:YAG crystal. This layout was chosen such that, in conjunction with edge focusing effects of the spectrometer dipole, the imaging condition for the electron beam is satisfied in both the horizontal and vertical planes at the YAG screen location for the design energy of 57 MeV. Direct measurement of the energy-resolved beam size $\sigma_y(E)$ in the plane of polarization over an energy bandwidth of 0.5 MeV was achieved. An example spectrometer image is shown in Fig. 2(a).

The characteristics of $\sigma_y(E)$ are determined by two factors: the electron beam transport (described above) and the initial transverse phase space of the electron beam. Using standard linear electron beam optics [29], the transport line can be expressed as the 6×6 matrix, $\mathbf{R}$, with the relevant elements to the vertical beam size being R_{33} and R_{34}. The energy dependence of the transfer matrix was also calculated. Within ± 1 MeV of the design energy, the elements of $\mathbf{R}$ have a predominantly linear dependence on E with $R_{33}(E) = 0.91(E - 57) - 14$ and $R_{34}(E) = 0.21(E - 57)$, where E is in units of MeV, R_{33} is unitless,

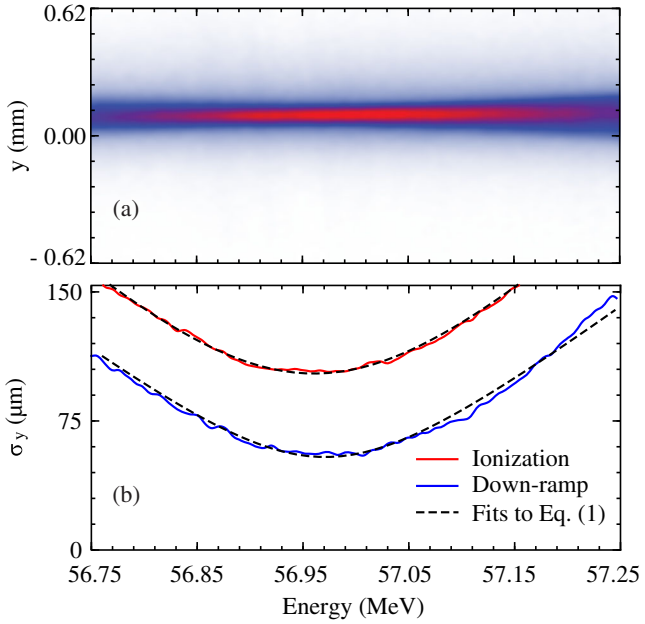

FIG. 2. (a) Single-shot image from the high-resolution YAG screen diagnostic showing energy-resolved vertical beam size of a down-ramp injected electron beam. (b) Measured beam size versus energy for the down-ramp injected beam shown (a) (blue line) and measurement from an ionization-injected beam with comparable spectral charge density (red line) with fits to Eq. (1) (black dashed lines).

and R_{34} is in units of m. The phase space in a single dimension is typically described using three parameters: a source size, a position or momentum correlation term, and the emittance. In the context of this measurement, however, we note that a nonzero position-momentum correlation simply results in shift of the $\sigma_y(E)$ curve by ΔE. This shift is easily identified in the measurements by noting the energy at which $\sigma_y(E)$ is minimized. It is also important to note that defocusing forces associated with space charge will also lead to a shift of the $\sigma_y(E)$ curve. Thus, the initial vertical phase space can be completely parametrized using the initial source size σ_{y0}, the emittance ϵ_y, and a focused energy shift term ΔE. Along with the R_{33} and R_{34} elements, $\sigma_y(E)$ is given by

$$\sigma_y(E) = \sqrt{[R_{34}(E^*)]^2\left(\frac{\epsilon_y}{\gamma\sigma_{y0}}\right)^2 + [R_{33}(E^*)]^2\sigma_{y0}^2}, \quad (1)$$

where $E^* = E - \Delta E$, and γ is the relativistic Lorentz factor.

While the optimized lattice presented above is relatively insensitive to second-order optics aberrations, experimentally it can be difficult to verify that the lattice is indeed fully optimized as intended. Accordingly, we consider the effect of small lattice errors and the resulting impact of second-order transport effects. To do this, $\sigma_y(E)$ is simulated including second-order optics for a variety of initial source parameters and lattice errors commensurate with the level of uncertainty in our experiment. The resulting $\sigma_y(E)$ is fit using Eq. (1). It was found that the lattice uncertainty, in conjunction with second-order effects, results in an overestimate of the emittance by $> 20\%$ only when the condition $\sigma_{y0}[\text{mrad}] \lesssim 1.5 + 2.0\epsilon_y[\text{mm mrad}]$ is not satisfied (and $< 20\%$ overestimate otherwise, which represents the vast majority of the data). It should be noted that a systematic effect of this type does not adversely affect a cross-comparison of the two injection methods, nor the measured charge dependences.

After the optimization and characterization of each LPA configuration on a separate larger field of view phosphor-based spectrometer screen, the electron beam was steered by increasing the dipole current to the high-resolution YAG screen diagnostic. A typical image is shown in Fig. 2(a), obtained using the down-ramp configuration. The beam size at each energy slice is determined by Gaussian fit after thresholding the profile at 50% of the peak value. This approach to defining the beam size excludes contributions from long tails in the distribution which can dominate the rms beam size while only containing a small fraction of the total charge. The blue line in Fig. 2(b) shows the beam size determined in this way for the image in Fig. 2(a), and the red line shows a beam size measurement of an ionization injection shot with a comparable spectral charge density. The emittance associated with each of these two measurements, determined by a fit to Eq. (1), is $1.0^{+0.2}_{-0.1}$ and $1.9^{+0.5}_{-0.2}$ mm mrad, roughly a factor of 2 larger for ionization injection. The error bars are determined by repeating the Gaussian fit of each energy lineout with thresholding values of 75% and 25%.

Results of emittance measurements taken from > 75 consecutive shots using each injection method are shown in Fig. 3(a). In addition to comparing the two injection schemes, the shot-to-shot variation in charge that arises from small fluctuations in laser properties permits a direct measurement of the dependence of emittance on charge density. Most notably, down-ramp injection consistently gives emittances smaller by roughly a factor of 2 compared to electron beams of the same charge densities produced via ionization injection.

For both cases there is a clear trend of increasing emittance with increasing charge density. With relatively low energy of the accelerated beam (< 100 MeV) and substantial total accelerated charge (86 ± 20 pC for ionization injection), the influence of space charge should be considered. In fact, one signature of a space charge effect is noted in a shift of the focused energy as a function of charge density, Fig. 3(b). Generally, the inclusion of space charge effects in the description of the transverse dynamics of the electron beam adds a defocusing term proportional to the generalized perveance, $K = I_b/I_A\beta^3\gamma^3$, where $I_A \approx 17$ kA is the Alfvén current, and β and γ are the relativistic factors. This effective reduction in focusing strength would cause a shift of the apparent focused energy towards lower

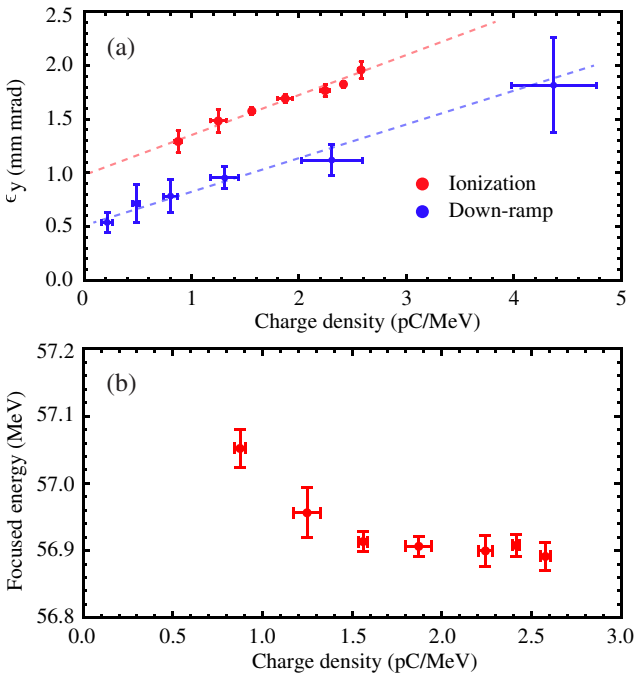

FIG. 3. (a) Emittance as a function of charge density for the two injection methods: ionization injection (red) and down-ramp injection (blue). The dashed lines are linear fits to guide the eye and can be used to extrapolate the space charge free emittance. (b) Dependence of focused energy on charge density for the ionization injection data.

energies for increasing charge, which is indeed evident in the data, Fig. 3(b). This direct evidence of a measurable space charge effect implies that the increasing emittance with charge density is in part due to space charge forces. Consequently, the measured emittance has contributions from both the intrinsic source emittance as well as space charge effects. Because space charge effects are highly sensitive to the initial beam parameters, in particular the bunch length, which are not simultaneously measured, it is not possible to accurately determine the space charge contribution to the emittance.

For both LPA configurations, the emittance dependence exhibits a highly linear dependence on charge density [indicated by the dashed lines in Fig. 3(a)]. Extrapolating these trends towards zero charge density can be used to estimate a space charge free emittance of 0.5 ± 0.1 and 1.0 ± 0.1 mm mrad for down-ramp and ionization injection, respectively. The trends indicate that although the space charge forces will likely be different for electron beams generated by the two different mechanisms and that the space charge likely contributes to the increasing emittance with increasing charge, it does not account for the difference in emittance between the two injection methods. Rather, the emittance is intrinsically larger for ionization injection in the polarization plane of the laser.

While the measured emittances are higher than what has been reported elsewhere [10,11,13], the measurements presented in this Letter were carried out at significantly higher spectral charge densities. Furthermore, the space charge effect, which was not relevant in Refs. [10,11,13], can be effectively suppressed by operating at higher energies (as in Ref. [13]), or by using a magnetic chicane placed close to the source to longitudinally stretch the electron beam and reduce the peak current.

A qualitative picture based on particle-in-cell (PIC) simulations provides valuable insight in comparing the two injection methods. Using a quasicylindrical PIC code [30], simulations were performed with laser and plasma parameters representative of the experimental conditions (described above). Figure 4 shows results for the two cases: Figs. 4(a) and 4(c) density down-ramp injection and Figs. 4(b) and 4(d) ionization injection. The green lines in Figs. 4(a) and 4(b) represent a sample of trajectories taken by injected electrons that reach a final accelerated energy of 55–60 MeV. For the down-ramp plot, the trajectories are plotted in terms of the radial coordinate r in order to emphasize that the trapped electrons originate from a narrow radial sheath that tracks along the outer edge of the bubble. In contrast, the trajectories for ionization injection are taken from narrow slices around $x = 0$ (top) and $y = 0$ (bottom) to highlight the differences between the trajectories in and out of the polarization plane. In both cases, the electrons originate on the right and slip backwards (to the left) in the simulation window comoving with the laser, until they are trapped near the back of the bubble.

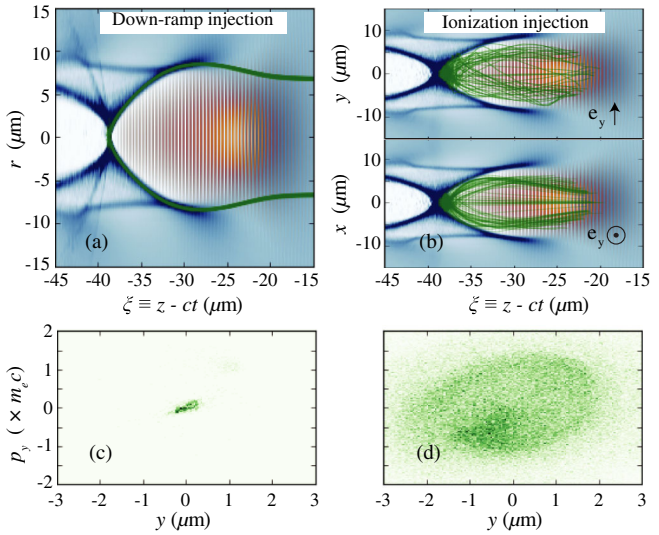

FIG. 4. Quasicylindrical PIC simulations showing the trajectories of trapped electrons (green lines) in down-ramp injection (a) and ionization injection (b). Laser polarization direction is indicated by $\mathbf{e}_y$. Transverse phase spaces of the electron in the 55–60 MeV bandwidth in the polarization direction at the end of the acceleration (c),(d).

We note a much larger variation in the trajectories taken by the ionization-injected electrons, which is due to the differences in both the laser phase at ionization and the ponderomotive force determined by the transverse positions of the injected electrons [31]. This gives rise to an increased spread in transverse momentum and initial spot size of the trapped beam and is the cause of the significantly different transverse phase space pictures for the two injection mechanisms, as can be seen in Figs. 4(c) and 4(d). Noting the considerably larger phase space area occupied by the ionization-injected electrons, and therefore emittance, these simulations suggest that with the considered plasma and laser parameters, down-ramp injection produces lower emittance electron beams, which is qualitatively consistent with the experimental results described above.

In summary, profiting from the high degree of flexibility afforded by the LPA setup, the two distinct injection mechanisms, shock-induced density down-ramp and ionization injection, were tuned and optimized to produce electron beams with the same central energy and peak spectral charge density. Combined with a carefully designed electron beam transport lattice and a high-resolution, single-shot, energy-resolved measurement of the vertical beam size, this allowed, for the first time, a direct and meaningful comparison of the transverse emittance of electron beams generated by the two mechanisms. We demonstrated that down-ramp injection produces beams with significantly better emittance compared to ionization injection, with emittances less than 0.5 mm mrad measured for down-ramp injection. Physically, simulations indicate

that the larger transverse emittance is due to the residual transverse momentum obtained as a result of electrons ionized near the peak of the laser pulse. These results mark a significant advance in the experimental characterization of LPA-produced electron beams.

This work was supported by the U.S. Department of Energy (DOE) under Contract No. DE-AC02-05CH11231, by the National Science Foundation under Grants No. PHY-1415596 and No. PHY-1632796, by the U.S. DOE National Nuclear Security Administration, Defense Nuclear Nonproliferation R&D (NA22), and by the Gordon and Betty Moore Foundation under Grant ID GBMF4898.

*sbarber@lbl.gov

[1] E. Esarey, C. B. Schroeder, and W. P. Leemans, Rev. Mod. Phys. **81**, 1229 (2009).
[2] K. Nalkajima, Nat. Phys. **4**, 92 (2008).
[3] A. R. Maier, A. Meseck, S. Reiche, C. B. Schroeder, T. Seggebrock, and F. Grüner, Phys. Rev. X **2**, 031019 (2012).
[4] Z. Huang, Y. Ding, and C. B. Schroeder, Phys. Rev. Lett. **109**, 204801 (2012).
[5] M. E. Couprie *et al.*, Plasma Phys. Controlled Fusion **58**, 034020 (2016).
[6] R. Hajima, N. Kikuzawa, N. Nishimori, T. Hayakawa, T. Shizuma, K. Kawase, M. Kando, E. Minehara, H. Toyokawa, and H. Ohgaki, Nucl. Instrum. Methods Phys. Res., Sect. A **608**, S57 (2009).
[7] O. Tesileanu, D. Ursescu, R. Dabu, and N. V. Zamfir, J. Phys. Conf. Ser. **420**, 012157 (2013).
[8] C. B. Schroeder, E. Esarey, C. G. R. Geddes, C. Benedetti, and W. P. Leemans, Phys. Rev. ST Accel. Beams **13**, 101301 (2010).
[9] S. Kneip, C. McGuffey, J. L. Martins, M. S. Bloom, V. Chvykov, F. Dollar, R. Fonseca, S. Jolly, G. Kalintchenko, K. Krushelnick, A. Maksimchuk, S. P. D. Mangles, Z. Najmudin, C. A. J. Palmer, K. T. Phuoc, W. Schumaker, L. O. Silva, J. Vieira, V. Yanovsky, and A. G. R. Thomas, Phys. Rev. ST Accel. Beams **15**, 021302 (2012).
[10] G. R. Plateau, C. G. R. Geddes, D. B. Thorn, M. Chen, C. Benedetti, E. Esarey, A. J. Gonsalves, N. H. Matlis, K. Nakamura, C. B. Schroeder, S. Shiraishi, T. Sokollik, J. van Tilborg, C. Toth, S. Trotsenko, T. S. Kim, M. Battaglia, T. Stöhlker, and W. P. Leemans, Phys. Rev. Lett. **109**, 064802 (2012).
[11] G. Golovin, S. Banerjee, C. Liu, S. Chen, J. Zhang, B. Zhao, P. Zhang, M. Veale, M. Wilson, P. Seller, and D. Umstadter, Sci. Rep. **6**, 24622 (2016).
[12] A. Cianchi, M. P. Anania, M. Bellaveglia, M. Castellano, E. Chiadroni, M. Ferrario, G. Gatti, B. Marchetti, A. Mostacci, R. Pompili, C. Ronsivalle, A. R. Rossi, and L. Serafini, Nucl. Instrum. Methods Phys. Res., Sect. A **720**, 153 (2013).
[13] R. Weingartner, S. Raith, A. Popp, S. Chou, J. Wenz, K. Khrennikov, M. Heigoldt, A. R. Maier, N. Kajumba, M. Fuchs, B. Zeitler, F. Krausz, S. Karsch, and F. Grüner, Phys. Rev. ST Accel. Beams **15**, 111302 (2012).
[14] N. Vafaei-Najafabadi, W. An, C. E. Clayton, C. Joshi, K. A. Marsh, W. B. Mori, E. C. Welch, W. Lu, E. Adli, J. Allen, C. I. Clarke, S. Corde, J. Frederico, S. J. Gessner, S. Z. Green, M. J. Hogan, M. D. Litos, and V. Yakimenko, Plasma Phys. Controlled Fusion **58**, 034009 (2016).
[15] C. McGuffey, A. G. R. Thomas, W. Schumaker, T. Matsuoka, V. Chvykov, F. J. Dollar, G. Kalintchenko, V. Yanovsky, A. Maksimchuk, K. Krushelnick, V. Y. Bychenkov, I. V. Glazyrin, and A. V. Karpeev, Phys. Rev. Lett. **104**, 025004 (2010).
[16] M. Chen, Z.-M. Sheng, Y.-Y. Ma, and J. Zhang, J. Appl. Phys. **99**, 056109 (2006).
[17] M. Chen, E. Esarey, C. B. Schroeder, C. G. R. Geddes, and W. P. Leemans, Phys. Plasmas **19**, 033101 (2012).
[18] A. Pak, K. A. Marsh, S. F. Martins, W. Lu, W. B. Mori, and C. Joshi, Phys. Rev. Lett. **104**, 025003 (2010).
[19] C. E. Clayton, J. E. Ralph, F. Albert, R. A. Fonseca, S. H. Glenzer, C. Joshi, W. Lu, K. A. Marsh, S. F. Martins, W. B. Mori, A. Pak, F. S. Tsung, B. B. Pollock, J. S. Ross, L. O. Silva, and D. H. Froula, Phys. Rev. Lett. **105**, 105003 (2010).
[20] S. Bulanov, N. Naumova, F. Pegoraro, and J. Sakai, Phys. Rev. E **58**, R5257 (1998).
[21] C. G. R. Geddes, K. Nakamura, G. R. Plateau, C. Toth, E. Cormier-Michel, E. Esarey, C. B. Schroeder, J. R. Cary, and W. P. Leemans, Phys. Rev. Lett. **100**, 215004 (2008).
[22] K. Schmid, A. Buck, C. M. S. Sears, J. M. Mikhailova, R. Tautz, D. Herrmann, M. Geissler, F. Krausz, and L. Veisz, Phys. Rev. ST Accel. Beams **13**, 091301 (2010).
[23] A. J. Gonsalves, K. Nakamura, C. Lin, D. Panasenko, S. Shiraishi, T. Sokollik, C. Benedetti, C. B. Schroeder, C. G. R. Geddes, J. van Tilborg, J. Osterhoff, E. Esarey, C. Toth, and W. P. Leemans, Nat. Phys. **7**, 862 (2011).
[24] A. Buck, J. Wenz, J. Xu, K. Khrennikov, K. Schmid, M. Heigoldt, J. M. Mikhailova, M. Geissler, B. Shen, F. Krausz, S. Karsch, and L. Veisz, Phys. Rev. Lett. **110**, 185006 (2013).
[25] K. K. Swanson, H. E. Tsai, S. K. Barber, R. Lehe, H. S. Mao, S. Steinke, J. van Tilborg, K. Nakamura, C. G. R. Geddes, C. B. Schroeder, E. Esarey, and W. P. Leemans, Phys. Rev. Accel. Beams **20**, 051301 (2017).
[26] J. van Tilborg, S. Steinke, C. G. R. Geddes, N. H. Matlis, B. H. Shaw, A. J. Gonsalves, J. V. Huijts, K. Nakamura, J. Daniels, C. B. Schroeder, C. Benedetti, E. Esarey, S. S. Bulanov, N. A. Bobrova, P. V. Sasorov, and W. P. Leemans, Phys. Rev. Lett. **115**, 184802 (2015).
[27] S. Steinke, J. van Tilborg, C. Benedetti, C. G. R. Geddes, C. B. Schroeder, J. Daniels, K. K. Swanson, A. J. Gonsalves, K. Nakamura, N. H. Matlis, B. H. Shaw, E. Esarey, and W. P. Leemans, Nature (London) **530**, 190 (2016).
[28] M. Fedurin, M. Babzien, V. Yakimenko, B. Allen, P. Muggli, and A. Murokh, in *Proceedings of the International Particle Accelerator Conference (IPAC'12), New Orleans, 2012* (IPAC 2012 Organizing committee/IEEE, New Orleans, 2012), paper MOP057, p. 2753.
[29] D. C. Carey, *The Optics of Charged Particle Beams* (Harwood Academic Publishers, New York, 1987).
[30] R. Lehe, M. Kirchen, I. A. Andriyash, B. B. Godfrey, and J.-L. Vay, Comput. Phys. Commun. **203**, 66 (2016).
[31] C. B. Schroeder, J.-L. Vay, E. Esarey, S. S. Bulanov, C. Benedetti, L.-L. Yu, M. Chen, C. G. R. Geddes, and W. P. Leemans, Phys. Rev. ST Accel. Beams **17**, 101301 (2014).